International Journal of Minerals, Metallurgy and Materials
Volume 22, Number 8, August 2015, Page 829
DOI: 10.1007/s12613-015-1140-9

Influence of chromium on the initial corrosion behavior of low alloy steels in the CO_2–O_2–H_2S–SO_2 wet–dry corrosion environment of cargo oil tankers

Qing-he Zhao[1)], *Wei Liu*[1)], *Jie Zhao*[2)], *Dong Zhang*[1)], *Peng-cheng Liu*[1)], *and Min-xu Lu*[1)]

1) Institute for Advanced Materials and Technology, University of Science and Technology Beijing, Beijing 100083, China
2) Marine Product Management Department, China Classification Society Headquarters, Beijing 100007, China
(Received: 15 December 2014; revised: 23 April 2015; accepted: 27 April 2015)

Abstract: The influence of Cr on the initial corrosion behavior of low-alloy steels exposed to a CO_2–O_2–H_2S–SO_2 wet–dry corrosion environment was investigated using weight-loss measurements, scanning electron microscopy, N_2 adsorption tests, X-ray diffraction analysis, and electrochemical impedance spectroscopy. The results show that the corrosion rate increases with increasing Cr content in samples subjected to corrosion for 21 d. However, the rust grain size decreases, its specific surface area increases, and it becomes more compact and denser with increasing Cr content, which indicates the enhanced protectivity of the rust. The results of charge transfer resistance (R_{ct}) calculations indicate that higher Cr contents can accelerate the corrosion during the first 7 d and promote the formation of the enhanced protective inner rust after 14 d; the formed protective inner rust is responsible for the greater corrosion resistance during long-term exposure.

Keywords: low alloy steels; corrosion rate; chromium; rust; oil tankers

1. Introduction

The inner gas in the vapor space of crude oil tankers (COTs) has been observed to contain oxygen (O_2), carbon dioxide (CO_2), sulfur dioxide (SO_2), hydrogen sulfide (H_2S), and water vapor originating from the crude oil being transported. An electrolyte film was observed to form and disappear on the backside of the upper deck because of the daytime/nighttime temperature changes. The pH value of this thin electrolyte film was approximately 2–4 because of the dissolution and chemical reaction of O_2, SO_2, and H_2S; thus, severe corrosion occurred [1]. The coexistence of H_2S, SO_2, O_2, and wet–dry cycles resulted in a unique corrosion environment. Some researchers have studied the corrosion behavior under these environmental conditions. For example, Kashima *et al.* [2] simulated the corrosion in the vapor space of COTs; they observed that the corrosion products were mainly composed of α-FeOOH, γ-FeOOH, Fe_3O_4, and elemental S and that the element S was enriched primarily in the outer rust layer. Soares *et al.* [3] investigated the effects of temperature and the concentration of CO_2 and H_2S on the corrosion behavior of ship steels subjected to the atmospheres encountered in COTs and established a corrosion wastage model based on a standard non-linear time-dependent corrosion model; they modified this model to account for the effects of different environmental factors in the COT atmosphere. Meanwhile, the development of low-alloy corrosion-resistant steels (LACRSs) for the upper deck of COTs has also been reported [4–5].

Small amounts of alloying elements such as Cu, Cr, and Ni have been incorporated into LACRS to enhance their atmospheric corrosion resistance. When LACRSs were exposed to a COT atmosphere, a homogeneous and adherent rust layer was formed on their surface [6–8]; this layer served as a protective barrier that inhibited the invasion of corrosive species [9–10]. Cr is one of the most important corrosion-resistant elements added to LACRSs. For example, the addition of Cr to weathering steels obviously improved their atmospheric corrosion resistance. Liu *et al.* [11] reported that Cr and Ni improved the corrosion resistance of the upper deck in the wet-gas environment of COTs and that the corrosion rate of the steels fluctuated with increasing

Corresponding author: Wei Liu E-mail: weiliu@ustb.edu.cn

testing time as the corrosion products formed and spalled. In the case of weathering steels exposed to industrial environments for prolonged periods, the surface rust with a duplex structure consisted predominantly of an outer rust layer of γ-FeOOH and an inner layer of nanosized α-FeOOH that contained a considerable amount of Cr [12]. Yamashita *et al.* [13], Asami and Kikuchi [14] studied the protective rust formed on weathering steel over an extended period and observed that Cr(Ⅲ) partly substituted for the Fe(Ⅲ) ions in α-FeOOH, which made the ion selectivity change from anion selectivity to cation selectivity; thus, the penetration of anions such as Cl^- was hindered. Their results also clarified that not only Cr but also Cu and Si were enriched in the inner rust layer. Kamimura and Stratmann [15] studied the corrosion rate of Cr-containing steels under wet/dry cycles using a Kelvin probe and observed that Cr inhibited the cathodic reaction during the transition process from wet to dry. In the oil and gas industry, a dense, amorphous, Cr-rich corrosion product is known to form to prevent the corrosion reaction of Cr-containing steels in electrolytes containing H_2S/CO_2 [16–18]. Furthermore, the effect of Cr on the mechanical properties and microstructure of LACRSs has also been investigated, as well as the relationship between mechanical properties and corrosion [19–20].

The corrosion conditions in the vapor space of COTs are unique and differ from those typically encountered in marine/industrial/rural atmospheric corrosion and in CO_2 corrosion in the oil and gas industry. Little research has been conducted on the influence of alloying elements on this kind of corrosion. Cr is one of the most important elements added to LACRSs to decrease their corrosion rate when exposed to corrosive atmospheres. Thus, clarification of how Cr affects the corrosion behavior of LACRSs exposed to the corrosive environment in the vapor space of COTs is important. However, to this point, the literature lacks relevant information about the influence of Cr content on the initial corrosion behavior of LACRSs, which is an impediment to the future development of novel LACRSs. In the present study, a CO_2–O_2–H_2S–SO_2 wet–dry cyclic corrosion environment was simulated using a homemade test device in accordance with IMO MSC 289(87) and the influence of various Cr contents on the initial corrosion behavior of LACRSs was investigated in detail.

2. Experimental

2.1. Composition of tested steels

Three kinds of LACRSs with various Cr contents and identical amounts of other elements were investigated in this work. The compositions of the tested steels are presented in Table 1. The samples were separated into 25 mm × 60 mm × 5 mm specimens for corrosion-rate measurements and into 10 mm × 10 mm × 5 mm specimens for surface and cross-section observations of the rusts. Furthermore, the length direction of the tested specimens was in accordance with the rolling direction and the surface exposed to the corrosive environment was nearby the rolling surface. The specimens were ground with SiC papers gradually down to 600# grade. After being cleaned with acetone and ethanol, the samples were stored in a desiccator for 24 h and then weighed on an electronic balance with an accuracy of 0.1 mg. The width and length of the exposure surface of the tested specimens were measured using vernier calipers with an accuracy of 0.02 mm.

Table 1. Chemical compositions of the tested steels wt%

Steel	C	Si	Mn	S	P	Cu	Ni	Cr	Fe
A	0.079	0.24	1.09	0.002	0.007	0.3	0.2	0.10	Bal.
B	0.075	0.24	1.05	0.002	0.006	0.3	0.2	0.17	Bal
C	0.071	0.24	1.04	0.002	0.006	0.3	0.2	0.48	Bal.

2.2. Simulated CO_2–O_2–H_2S–SO_2 wet–dry corrosion tests

A schematic of the test device used to simulate the complicated CO_2–O_2–H_2S–SO_2 wet–dry corrosion environment in the vapor space of COTs according to IMO MSC 289(87) is shown in Fig. 1; the test device was mainly composed of a temperature control system, a water-bath, and a gas pipeline. The tested specimens were maintained at 50°C for 19 h and 25°C for 3 h and subsequently subjected to the corrosive conditions for 1 h at temperatures between 50°C and 25°C. One cycle required 24 h, and the total corrosion time was 21 d. The temperature of distilled water in the container was maintained between 31°C and 34°C. The inlet gas was composed of 13% CO_2, 4% O_2, 500×10^{-6} H_2S, and 100×10^{-6} SO_2 with N_2 balance. A sufficient distance of 180 mm between the corrosion surface of the specimens and distilled water was maintained to avoid splashing of the distilled water. The minimum gas flow rate was 100 mL/min for the first 24 h and then 20 mL/min after 24 h. Thus, the test device could well simulate the conditions of the actual inner space of COTs.

2.3. Corrosion-rate measurements

For corrosion-rate measurements, the rust layers were removed mechanically and chemically in pickling solution (500 mL HCl + 500 mL H_2O + 3.5 g $C_6H_{12}N_4$) in accordance

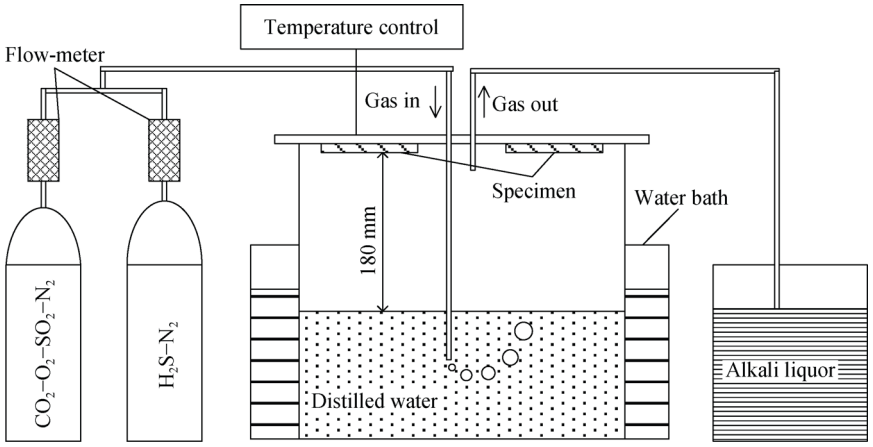

Fig. 1. Schematic of the test device used to simulate the corrosion environment in the vapor space of COTs.

with standard ASTM G1–03, then cleaned and dried in ethanol and weighed on an electronic balance with an accuracy of 0.1 mg. The corrosion losses of the tested specimens were calculated by

$$\mathrm{CR} = \frac{3650 \times (W_0 - W_1)}{\mathrm{CT} \times S \times D} \quad (1)$$

where CR is the corrosion rate (mm/a), CT is the corrosion time (d), W_1 is the specimen's weight after corrosion (g), W_0 is the weight of the specimen before corrosion (g), S is the corrosion area (cm^2), and D is the density of the tested steel (D = 7.85 g/cm^3).

2.4. Rust morphology and composition analyses

The surface and cross-section morphologies of rusts were characterized by scanning electron microscopy (SEM, LEO 1450), and the compositions of the rusts were analyzed using an internal-standard X-ray diffraction (XRD) method on an instrument equipped with a Cu target. Rusts were stripped mechanically and carefully collected. Rust powder samples were prepared for quantitative phase analysis. The XRD scan speed was 2.0°/min, and the 2θ range was 10° to 50°. XRD analysis consisted of both qualitative and quantitative analysis. ZnO was used as an internal standard for the quantitative analysis [21–22], whereas the qualitative analysis was performed without ZnO. The crystalline rust phases were goethite (α-FeOOH), lepidocrocite (γ-FeOOH), magnetite (Fe_3O_4), and elemental S. The diffraction intensities of the (011) reflection of α-FeOOH, the (020) reflection of γ-FeOOH, the (220) reflection of Fe_3O_4, and the (222) reflection of elemental S were measured and compared with the (100) reflection of ZnO powder. The ZnO/rust ratio was 3:7.

2.5. N_2 adsorption tests

The adsorption isotherms of N_2 for rusts were measured at the boiling point of liquid N_2 using an AUTOSORB–6B. Samples were degassed at 100°C under 133.3227×10^{-3} Pa for 2 h before the tests. The specific surface area (SSA) of rusts was determined by fitting the Brunauer–Emmett–Teller (BET) equation to the adsorption isotherms using the cross-sectional area (0.162 nm^2) of the N_2 molecule.

2.6. EIS measurements

For electrochemical impedance spectroscopy (EIS) measurements, a three-electrode system was used. The working electrode was bare steel or rusted specimens, the reference electrode was a saturated calomel electrode, and the auxiliary electrode was a platinum electrode. The tests were conducted at 25°C and at pH 3.0 in 0.1 mol/L Na_2SO_4 solution. EIS measurements were conducted using a CHI 660D electrochemical workstation; the frequency ranged from 100 kHz to 10 mHz, and the signal amplitude was 5 mV. The measured EIS data were fitted using the ZSimpWin software.

3. Results and discussion

3.1. Corrosion rates of the three steels

The corrosion rates (CR, mm/a) for Cr-containing LACRSs exposed for 21 d to a simulated CO_2–O_2–H_2S–SO_2 wet–dry cyclic corrosion environment designed to simulate the vapor space of COTs are shown in Fig. 2. The results show that the CR of the LACRSs increased as the Cr content was increased from 0.1wt% to 0.48wt%. Compared to the designed 25-year service life, corrosion in 21 d represents the initial corrosion stage, and the results show that increasing Cr content can accelerate corrosion during the initial corrosion stage when the specimen is exposed to a CO_2–O_2–H_2S–SO_2 wet–dry cyclic corrosion environment designed to simulate the vapor space of COTs.

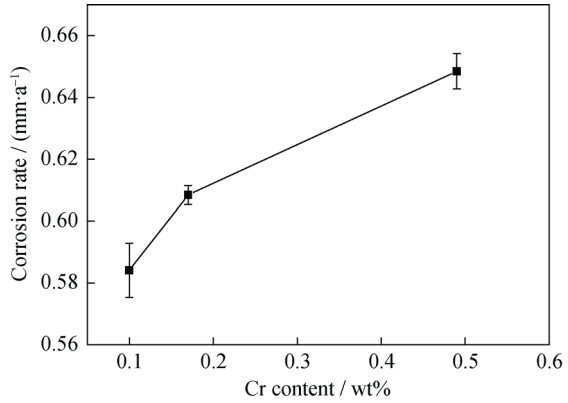

Fig. 2. Corrosion rate of LACRSs with different Cr contents exposed for 21 d to the CO_2–O_2–H_2S–SO_2 wet–dry cyclic corrosion environment designed to simulate the vapor space of COTs.

3.2. Rust characterization

Fig. 3 shows the surface appearance of the rusts formed on three LACRS with different Cr contents when the specimens were exposed for 21 d to the CO_2–O_2–H_2S–SO_2 wet–dry cyclic corrosion environment designed to simulate the vapor space of a COT. The surface of the rusts exhibits red-brown round or elliptic corrosion products distributed on a dark-rust substance. The color of the rust layer is related to the rust phases. Usually, rusts formed on the steel via atmospheric corrosion are composed mainly of ferric oxyhydroxides (FeOOH) and an X-ray-amorphous phase that does not give a well-defined Bragg peak [23–24]. The crystalline rust phases are γ-FeOOH, which is yellow-orange and α-FeOOH, which is dark-brown [25–26]. We inferred from Fig. 3 that the red-brown round regions of the rust phases are composed mainly of crystalline α-FeOOH and γ-FeOOH, whereas the dark substance is mainly X-ray-amorphous rust compounds.

The surface morphologies of rusts formed in the CO_2–O_2–H_2S–SO_2 wet–dry cyclic corrosion environment are shown in Fig. 4. As evident in Figs. 4(a), 4(b), and 4(c), the rusts are compact and adherent to the substrate, with quite similar morphologies. The rust surfaces are divided into two parts: the compact parts coincide with the dark substrate, and the tough, round parts coincide with the red-brown region shown in Fig. 4. Because of the small grain size of the iron phase, we observed the morphology of the rust layer at high magnification, as shown in Figs. 4(d) to 4(i). Figs. 4(d), 4(e), and 4(f) show the surface morphologies of the compact parts. These results indicate that no obvious difference exists between the three kinds of LACRSs. Figs. 4(g), 4(h), and 4(i) show the surface morphologies of the tough, round parts, whose sections appear as aggregates of worms in different grain sizes among the three LACRSs. As evident in these figures, the grain size decreased with increasing Cr content.

The cross-sectional morphologies of the rusts for three tested steels exposed to the CO_2–O_2–H_2S–SO_2 wet–dry cyclic corrosion environment for 21 d were investigated by SEM; the results are shown in Fig. 5. Figs. 5(a) and 5(b)

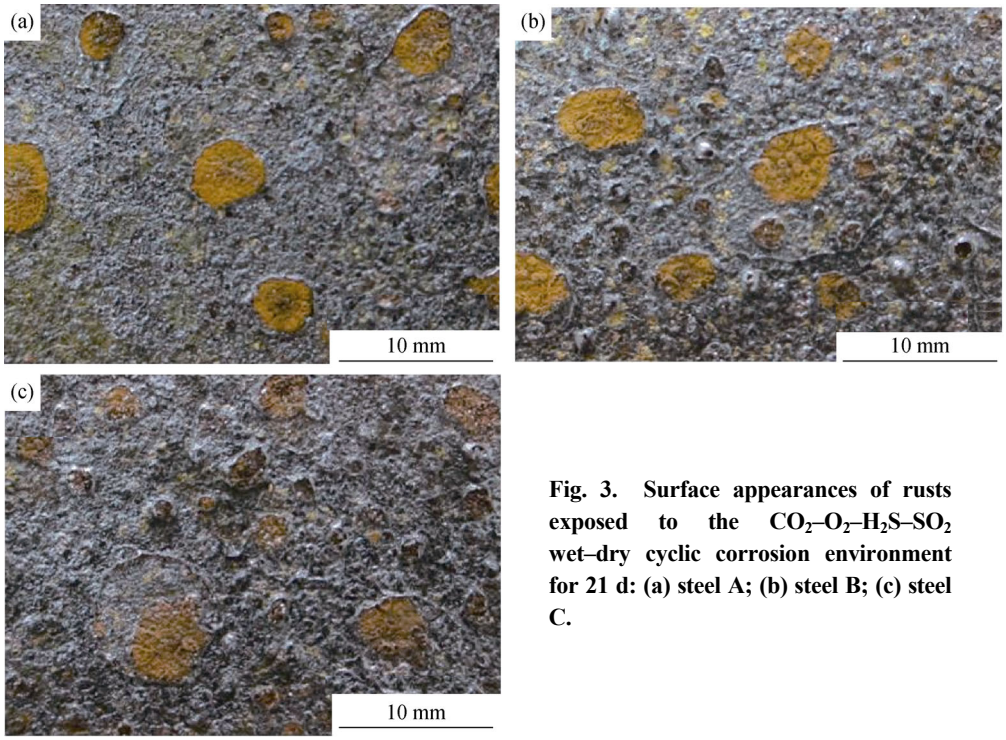

Fig. 3. Surface appearances of rusts exposed to the CO_2–O_2–H_2S–SO_2 wet–dry cyclic corrosion environment for 21 d: (a) steel A; (b) steel B; (c) steel C.

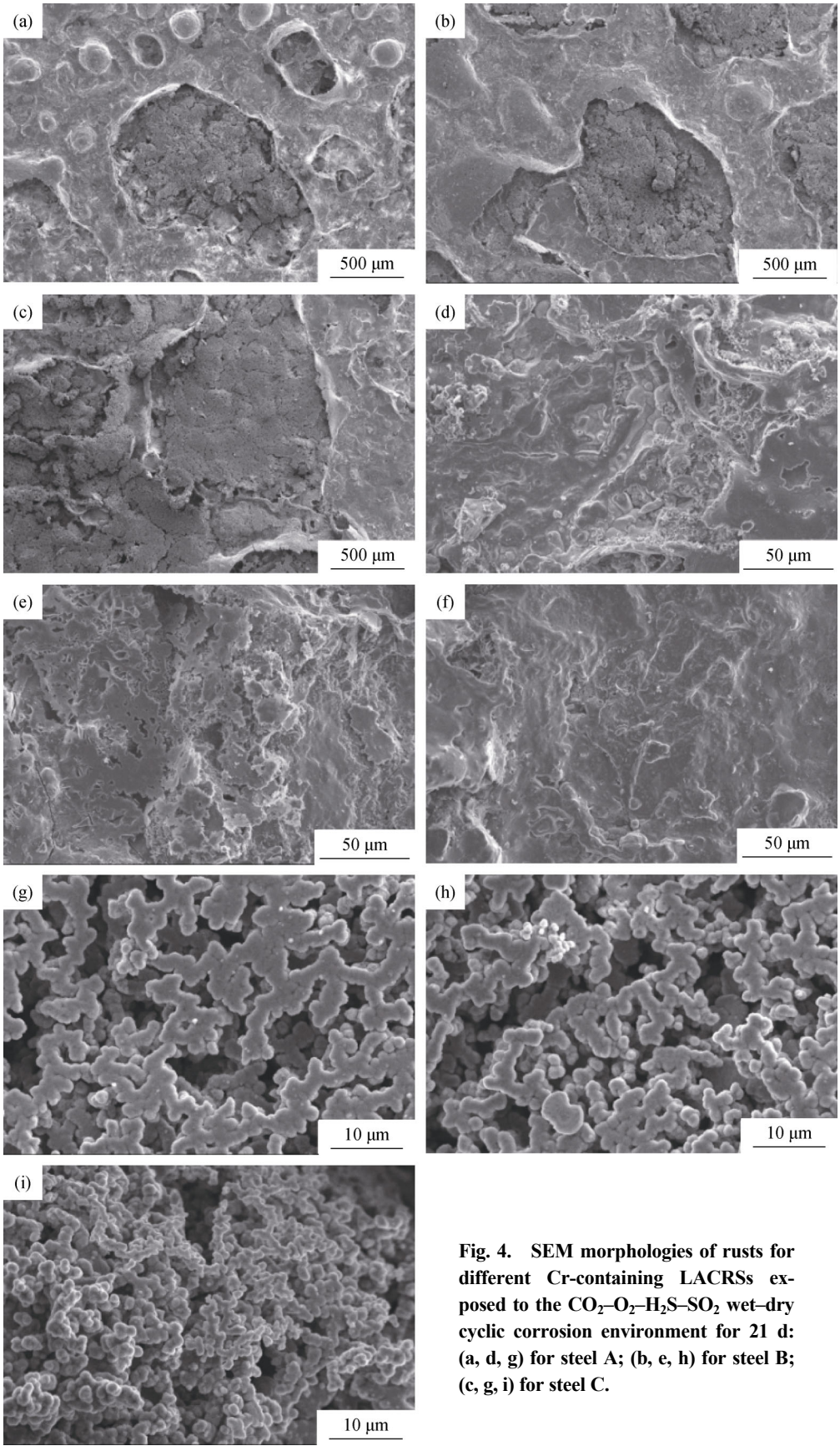

Fig. 4. SEM morphologies of rusts for different Cr-containing LACRSs exposed to the CO_2–O_2–H_2S–SO_2 wet–dry cyclic corrosion environment for 21 d: (a, d, g) for steel A; (b, e, h) for steel B; (c, g, i) for steel C.

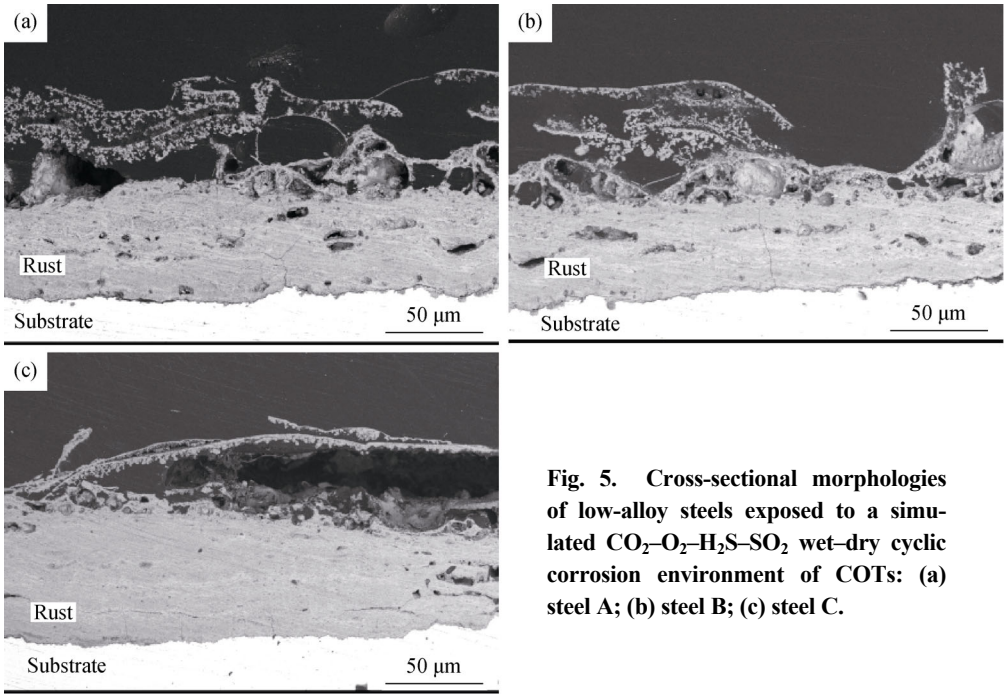

Fig. 5. Cross-sectional morphologies of low-alloy steels exposed to a simulated CO_2–O_2–H_2S–SO_2 wet–dry cyclic corrosion environment of COTs: (a) steel A; (b) steel B; (c) steel C.

show that the characteristics of the rusts formed on steel A and steel B are similar in that they both exhibit numerous flaws such as cracks and pores and nearly identical thicknesses; however, they also exhibit slight differences. Specifically, the rust of steel B is more compact and the interface between the rust layers and the substrate is more even than that of steel A. The corrosion rate of steel C is the highest among the three steels, which results in the largest amount of iron atoms entering into the rust, resulting in steel C exhibiting the thickest and most compact rust among the investigated specimens, as shown in Fig. 5(c). Consequently, the increasing Cr content in the steels may be the major reason for steel C exhibiting different corrosion behavior under the simulated COT environment.

Fig. 6 shows the XRD patterns of rusts formed on three different Cr-containing LACRSs exposed to the CO_2–O_2–H_2S–SO_2 wet–dry cyclic corrosion environment for 21 d. These results reveal that the phase constitutions of the rusts are similar and that they are mainly composed of crystalline α-FeOOH, γ-FeOOH, Fe_3O_4, and elemental S. This qualitative phase analysis is similar to the results reported by Shiomi *et al.* [1] and by Kashima *et al.* [2], although some differences were noted. A low concentration of H_2S was used in this investigation compared to the 500×10^{-6}–3000×10^{-6} H_2S in actual COTs [3] and the 2000×10^{-6} H_2S used in the study by Kashima *et al.* [2]; thus, the diffraction peak of elemental S in the present work is not obvious, whereas nearly 60wt% of elemental S has been observed in actual COTs [1].

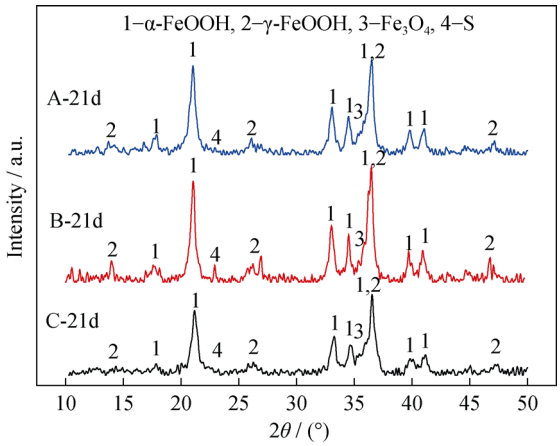

Fig. 6. XRD patterns of rusts for three various Cr-containing LACRSs exposed to the CO_2–O_2–H_2S–SO_2 wet–dry cyclic corrosion environment for 21 d.

Table 2 shows the results of the quantitative phase analysis of rusts; as evident in the table, the rusts contains large amounts of X-ray-amorphous rust compounds, which are composed mainly of microcrystalline oxides or hydroxides and could not be identified by XRD [12,27]. A comparison of the rust phases formed on three Cr-containing LACRSs reveals that the quantities of α-FeOOH and γ-FeOOH decrease slightly, whereas the quantities of Fe_3O_4 and amorphous compounds increase; the quantity of elemental S exhibited irregular changes with increasing Cr content in the LACRSs. These results indicate that a higher Cr content can promote the formation of Fe_3O_4 and amorphous rust compounds and inhibit formation of α-FeOOH and γ-FeOOH.

Table 2. Quantitative XRD phase analysis of rusts formed on three different Cr-containing LACRSs exposed to the CO_2–O_2–H_2S–SO_2 wet–dry cyclic corrosion environment for 21 d wt%

Specimen	Cr	α-FeOOH	γ-FeOOH	Fe_3O_4	Element S	Amorphous rust
Steel A-21d	0.10	6.3	14.6	2.0	1.0	76.1
Steel B-21d	0.17	5.5	13.5	2.7	1.4	76.9
Steel C-21d	0.48	5.6	11.9	3.4	0.9	78.2

3.3. N_2 adsorption results

Fig. 7 shows specific surface area (SSA) results for the rusts of the three LACRSs exposed to the CO_2–O_2–H_2S–SO_2 wet–dry cyclic corrosion environment for 21 d. As evident in the figure, the SSA increases with increasing corrosion time. Ishikawa *et al.* [28] noted that finer corrosion products are advantageous for the protection performance of rust layers. Finer corrosion products result in a larger SSA. We determined the SSA of the corrosion products by measuring their N_2 adsorption isotherms. The XRD results summarized in Table 3 indicate that the proportion of X-ray-amorphous compounds in the rusts reached nearly 80wt%, which is substantially greater than the proportions of the crystalline phases. The X-ray-amorphous compounds are mainly composed of microcrystalline oxides or hydroxides [13,27]. Furthermore, their size is one of the key parameters for determining the protection ability of rust layers. In this study, the X-ray-amorphous compounds are mainly responsible for the SSA of the rust layers. The amount of amorphous rust increases with increasing Cr content, which contributes to the increasing SSA. The SSA results indicate that the higher Cr content is responsible for formation of finer rust and for the greater protection ability of the rust.

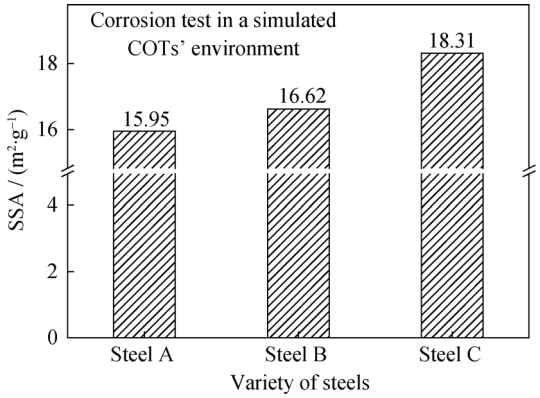

Fig. 7. SSA of rusts of LACRSs exposed to the simulated COT environment for 21 d.

3.4. Electrochemical measurements

Fig. 8 shows the Nyquist plots (Fig. 8(a)) and Bode plots (Fig. 8(b)) for three different Cr-containing bare steels whose electrochemical properties were measured in pH 3.0, 25°C, 0.1 mol/L Na_2SO_4 solution. The Nyquist plots are composed of one capacitive reactance arc in the high-frequency region and an inductance arc in the low-frequency region. Accordingly, a proposed general equivalent electrical circuit is depicted in Fig. 9. In the equivalent circuit, R_s represents the electrolyte resistance; R_{ct} represents the charge transfer resistance in the substrate/rust interface; Q_{dl} represents the double-layer capacitance as a constant phase-angle element (CPE), which is the admittance caused by non-Faraday processes resulting from the roughness of the electrode surface and energy dissipation; R_L represents the electrical inductance; and L represents the inductance element. The value of electrochemical parameters obtained from the equivalent circuit of the EIS data are shown in Table 3. And in the table, n_{dl} represents the deviation of the double layer from the ideal capacitor in the electrode interface, and its values are between 0 and 1. As detailed in the

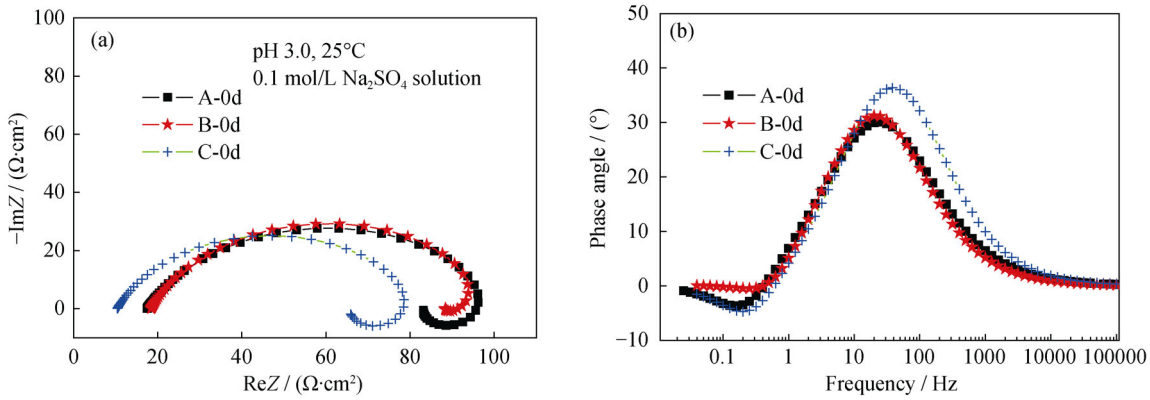

Fig. 8. Nyquist and Bode plots of Cr-containing bare steels in a pH 3.0, 25°C, 0.1 mol/L Na_2SO_4 solution: (a) Nyquist plots; (b) Bode plots.

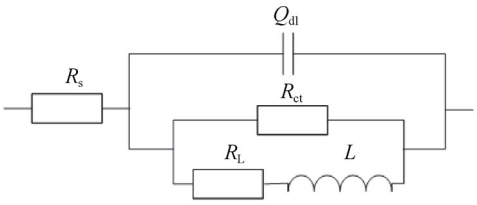

Fig. 9. Equivalent circuit used for fitting the EIS data of low-alloy steels in pH 3.0, 25°C, 0.1 mol/L Na_2SO_4 solution.

Table 3. Electrochemical parameters of bare steels fitted with the measured EIS data

Sample	Q_{dl} / ($\mu F \cdot cm^{-2}$)	n_{dl}	R_{ct} / ($\Omega \cdot cm^2$)	R_L / ($\Omega \cdot cm^2$)	L / ($H \cdot cm^{-2}$)
Steel A	743.4	0.726	86.8	273.1	230.9
Steel B	669.2	0.764	86.4	379.1	117.1
Steel C	578.4	0.764	73.6	223.2	159.1

table, the R_{ct} and Q_{dl} of steel C are lower than those of steels A and B. This result indicates that increasing Cr content adversely affects the corrosion resistance of the bare steel.

Fig. 10 shows the Nyquist plots (Figs. 10(a), 10(c), and 10(e)) and Bode plots (Figs. 10(b), 10(d), and 10(f)) obtained in pH 3.0, 25°C, 0.1 mol/L Na_2SO_4 solution for the rusted steel corroded for 7, 14, and 21 d, respectively. As evident in the figure, the Nyquist plots are composed of a depressed semicircle in the high-frequency region and another depressed semicircle coexisting with a long tail in the low-frequency region. Generally, the charge transfer resistance at the rust/steel interface dominates at low frequencies and the resistance of the rust dominates at high frequencies [21,29]. Accordingly, an equivalent electrical circuit for the rusted steels is proposed as depicted in Fig. 11. In the

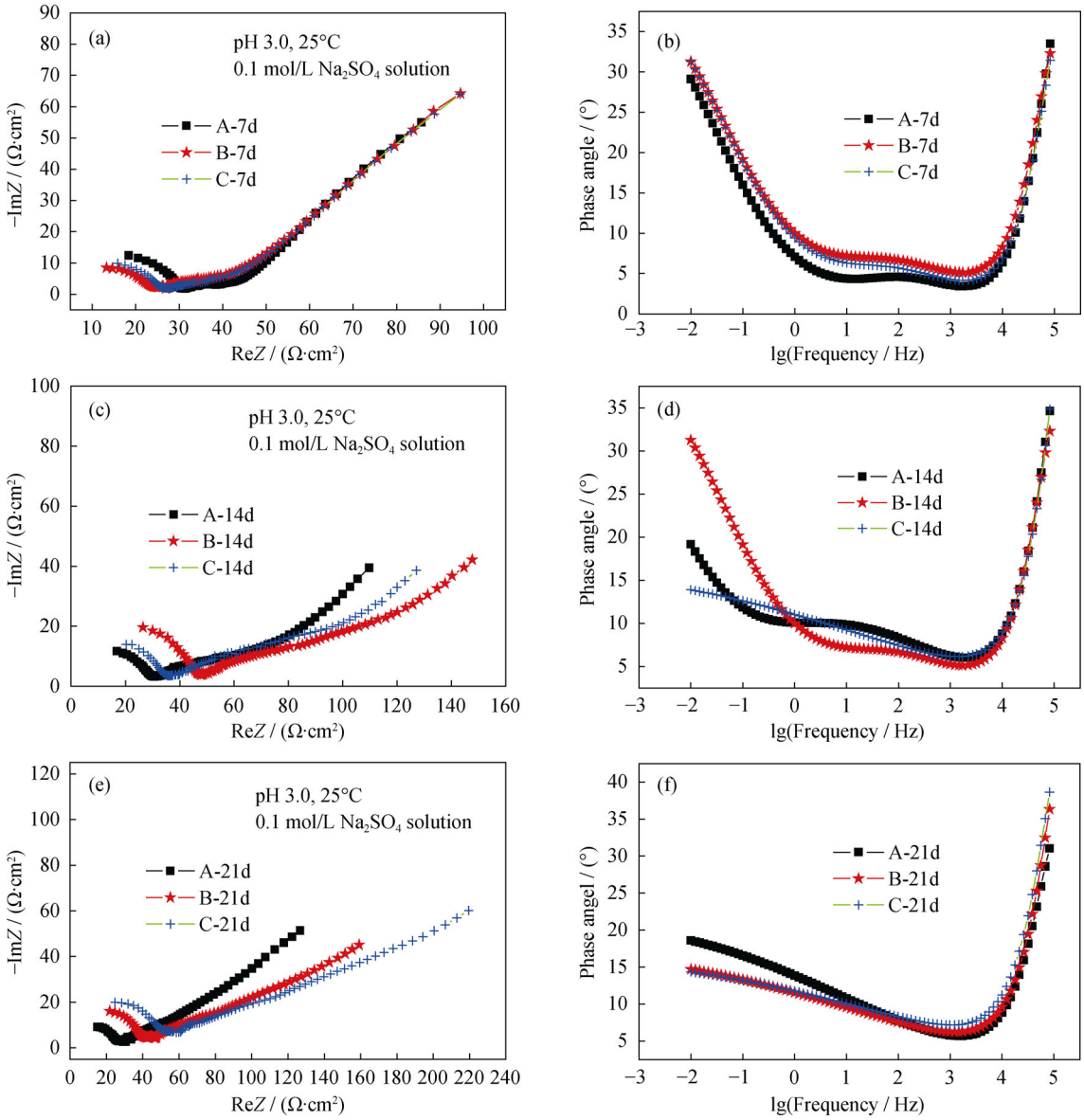

Fig. 10. Nyquist and Bode plots of three rusted LACRSs in a pH 3.0, 25°C, 0.1 mol/L Na_2SO_4 solution.

equivalent circuit, R_s represents the electrolyte resistance; R_{rust} and Q_{rust} represent the resistance and capacitance of the rust layer, respectively; R_{ct} represents the charge transfer resistance associated with both the anodic reaction and the cathodic reaction; Q_{dl} represents the double-layer capacitance as a CPE; and Z_w represents is the barrier diffusion impedance, which is associated with diffusion of corrosive electrolyte to the steel surface through pores in the rust, where the rust acts as a diffusion barrier. The ZsimpWin software and equivalent circuits in Fig. 11 were used to calculate and simulate the EIS data; the errors are guaranteed to be less than 10%. The electrochemical parameters of the rusted specimens for steel A, steel B, and steel C are shown in Table 4.

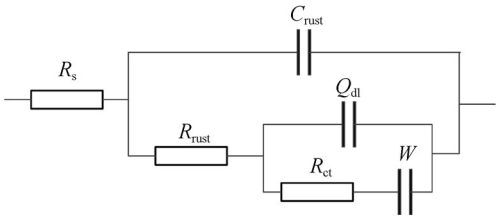

Fig. 11. Equivalent circuit for rusted steels in a pH 3.0, 25°C, 0.1 mol/L Na_2SO_4 solution.

The evolution of R_{rust} and R_{ct} of the rusted specimens is shown in Fig. 12. The results from Fig. 12(a) indicate that the value of R_{rust} for steels B and C increases with increasing corrosion time, whereas the value of R_{rust} for steel A remains nearly unchanged. In this study, no obvious interface was observed between the outer rust layer and the inner rust layer; thus, R_{rust} and Q_{rust} represent the resistance and capacitance of the rust layer in which the outer rust and inner rust are considered as a whole. The change in R_{rust} indicates that a higher Cr content in steels may be advantageous to the formation of a compact rust layer with enhanced corrosion resistance, which is consistent with the results presented in Figs. 4 and 5.

Table 4. Electrochemical parameters of three rusted LACRSs with various Cr contents

Steel	C_{rust} / ($nF \cdot cm^{-2}$)	R_{rust} / ($\Omega \cdot cm^2$)	Q_{dl} / ($mF \cdot cm^{-2}$)	n_{dl}	R_{ct} / ($\Omega \cdot cm^2$)
A-7d	73	24.0	2.5	0.559	20.8
A-14d	73	23.2	9.2	0.297	95.3
A-21d	38	25.6	13.0	0.311	166.3
B-7d	13	18.1	5.1	0.429	18.5
B-14d	56	29.9	7.8	0.305	116.5
B-21d	55	27.8	10.3	0.238	240.3
C-7d	98	16.6	5.1	0.451	16.2
C-14d	42	23.9	8.3	0.289	152.5
C-21d	46	36.7	8.4	0.187	354.6

Fig. 12(b) reveals that the value of R_{ct} decreased approximately 55 to 65 $\Omega \cdot cm^2$ from 0 to 7 d and then increased substantially from 7 to 21 d for all of the tested steels. The difference of the cathodic process between bare steels and rusted steels may contribute to this result. In Fig. 8, for bare steels, the cathodic process is controlled by the reduction of H^+ and dissolved O_2 [7,24,28], whereas the anodic process is controlled by the steel dissolution. However, for the rusted steel, the reduction of rusts becomes the dominant process and the reduction of the dissolved O_2 becomes the secondary process [7,30]. Furthermore, the R_{ct} at 7 d decreases with increasing Cr content in the steels, whereas the R_{ct} at 14 and 21 d increases. Because the behaviors of R_{ct} and Q_{dl} are closely related to the properties of the inner rust that is adherent to the steel substrate, these R_{ct} results indicate that steel C exhibits enhanced inner rust protectivity with increasing corrosion time.

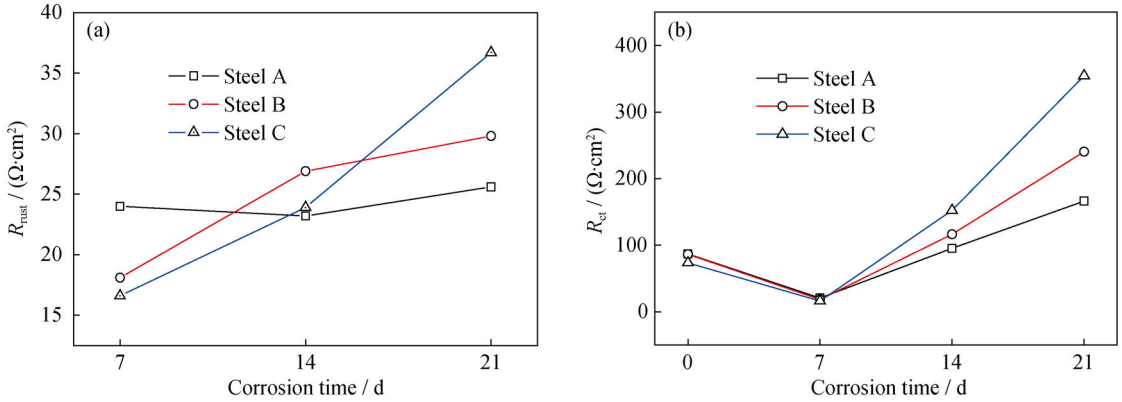

Fig. 12. Evolution of rust resistance (R_{rust}) and charge transfer resistance (R_{ct}) of LACRSs exposed to CO_2–O_2–H_2S–SO_2 wet–dry cyclic environment as a function of corrosion time (CT): (a) R_{rust}–CT; (b) R_{ct} –CT.

3.5. Discussion

The corrosion rates and corrosion losses of different Cr-containing LACRSs corroded for 21 d increased with increasing Cr content under the CO_2–O_2–H_2S–SO_2 wet–dry cyclic corrosion environment. Corrosion for 21 d represents the initial corrosion stage relative to the designed 25-year service life of cargo oil tankers. The R_{ct} of steel C in its bare state and that of steel C corroded for 7 d are the lowest R_{ct} values among the three tested steels, which indicates that the low-alloy steels with high Cr contents tend to exhibit high corrosion rates during the initial corrosion stage. This high corrosion rate may contribute to the largest corrosion loss of steel C. After corrosion for 14 and 21 d, the R_{ct} of steel C remained the highest among the three steels, which indicates that a compact and protective inner rust layer was formed on the surface of steel C.

The influence of Cr on rust evolution and on the formation of a compact and protective rust layer during the initial stage of corrosion is explained as follows. Cr^{3+} is generated by the anodic reaction of low-alloy steels ($Cr \rightarrow Cr^{3+} + 3e^-$) and reacts with OH^- to form the precipitate $Cr(OH)_3$ because of the low solubility of Cr^{3+} in the presence of OH^- [31–32]. The $Cr(OH)_3$ is subsequently transformed to $Cr(O,OH)_6$ or CrO_x, which can serve as the nucleation core for the formation of crystalline γ-FeOOH or amorphous rust particles [33–34]. The generation of more $Cr(O,OH)_6$ or CrO_x cores enables the formation of more rust particles; thus, the grain size of the corrosion products is smaller for the steels with higher Cr contents. This tendency can explain that the grain size of the aggregates of worms decreased with increasing Cr content in the steel (Fig. 3) and that the SSA increased with increasing Cr content (Fig. 6).

The rust phase composition after 21 d of corrosion was also affected by alloyed Cr. The results in Table 3 imply that the quantities of α-FeOOH and γ-FeOOH decreased and the quantities of Fe_3O_4 and amorphous compounds increased with increasing Cr content in steels corroded for 21 d. Higher Cr contents can reduce the formation of γ-FeOOH and promote the formation of amorphous rust compounds. γ-FeOOH formation was dominant during the initial stage of exposure, and it likely gradually transformed to α-FeOOH under the acid electrolyte film [7]. Furthermore, the co-existence of Fe^{2+} diffused from the inner rust and SO_4^{2-} from the outer atmosphere accelerated the transformation process from ferric oxide to α-FeOOH in an low-pH COT environment [35–36]. The α-FeOOH content decreased slightly with increasing Cr content in the steels, which may indicate that the formation of α-FeOOH was affected primarily by the corrosion circumstances rather than by the Cr content in the steels. A certain amount of H_2S and O_2 in the corrosion atmosphere dissolved into the electrolyte film and reacted with each other; thus, the elemental S precipitated in the surface of the rust layer. The amount of elemental S was also affected primarily by the atmospheric conditions rather than by the Cr content. For the formation of Fe_3O_4, either a reducing condition near the metal surface or an insufficient supply of oxygen is necessary; thus, Fe_3O_4 is more likely to form during the initial stage of corrosion in contact with metal surfaces [7]. For the rusts collected after 21 d of corrosion in this study, more compact and denser rust layers resulted in smaller amounts of oxygen diffused into the inner rust, which contributed to the rust layer of steel C containing the largest amount of Fe_3O_4.

In this study, the amount of γ-FeOOH in the rust was consistent with the electrochemical properties of the rusted specimens, as shown in Table 4. The amount of electrochemically active γ-FeOOH decreased with increasing Cr content in the LACRSs during the early stage of corrosion. γ-FeOOH can be used as a cathodic depolarization agent to participate in the cathodic process and accelerate the corrosion of the steel substrate [37–38], as shown in

$$Fe^{2+} + 8\gamma\text{-FeOOH} + 2e^- \rightarrow 3Fe_3O_4 + 4H_2O \quad (2)$$

The R_{rust} and R_{ct} of rusted steels after 21 d of corrosion increased with increasing Cr content; i.e., the protective ability of the rust layer increased with increasing Cr content in the LACRSs. The decrease in the amount of γ-FeOOH with increasing Cr content may contribute to this enhanced protective ability from an electrochemical viewpoint.

The R_{ct} values of the bare steels decreased with increasing Cr content because of the thermodynamic stability of the steel substrate. The R_{ct} after 7 d of corrosion was much smaller than that of bare steels because the electrochemically active corrosion products (e.g., γ-FeOOH) participate in the cathodic reaction as a cathodic depolarization agent. The R_{ct} values were much larger than the R_{rust} values in all of the tested specimens subjected to 14 d and 21 d of corrosion. Evaluating the rust protectivity by the R_{ct} rather than the R_{rust} is preferable because the compact inner rust layer is believed to be mainly responsible for the corrosion resistance of rusted steels. With increasing Cr content, the R_{ct} values of the specimens subjected to 21 d of corrosion increased gradually and were substantially larger than the R_{ct} value of the bare steel. The R_{ct} value of the steel with the highest Cr content (steel C, 0.48wt% Cr) was 2.1 and 1.4 times greater than the values of steel A (0.1wt% Cr) and steel B (0.17wt% Cr), which indicates that the alloyed Cr can significantly

improve the inhibition effect of electrochemical reaction at the substrate/rust interface.

An increase in Cr content of the LACRSs improved the value of R_{ct} because of the formation of high-corrosion-resistance rust; thus, the inhibition of electrochemical reactions at the rust/substrate interface was enhanced. The R_{rust} value slightly changed and the R_{ct} significantly increased with increasing corrosion time (Fig. 12), and the value of R_{ct} was an order of magnitude greater than that of R_{rust} (Fig. 13). The R_{ct} and R_{rust} values indicate that an increase in Cr content can improve the corrosion rate and promote the formation of rust in the initial corrosion stage; thus, the R_{ct} in the rust/substrate interface is enhanced, which is beneficial to lowering the long-term corrosion rate of steels.

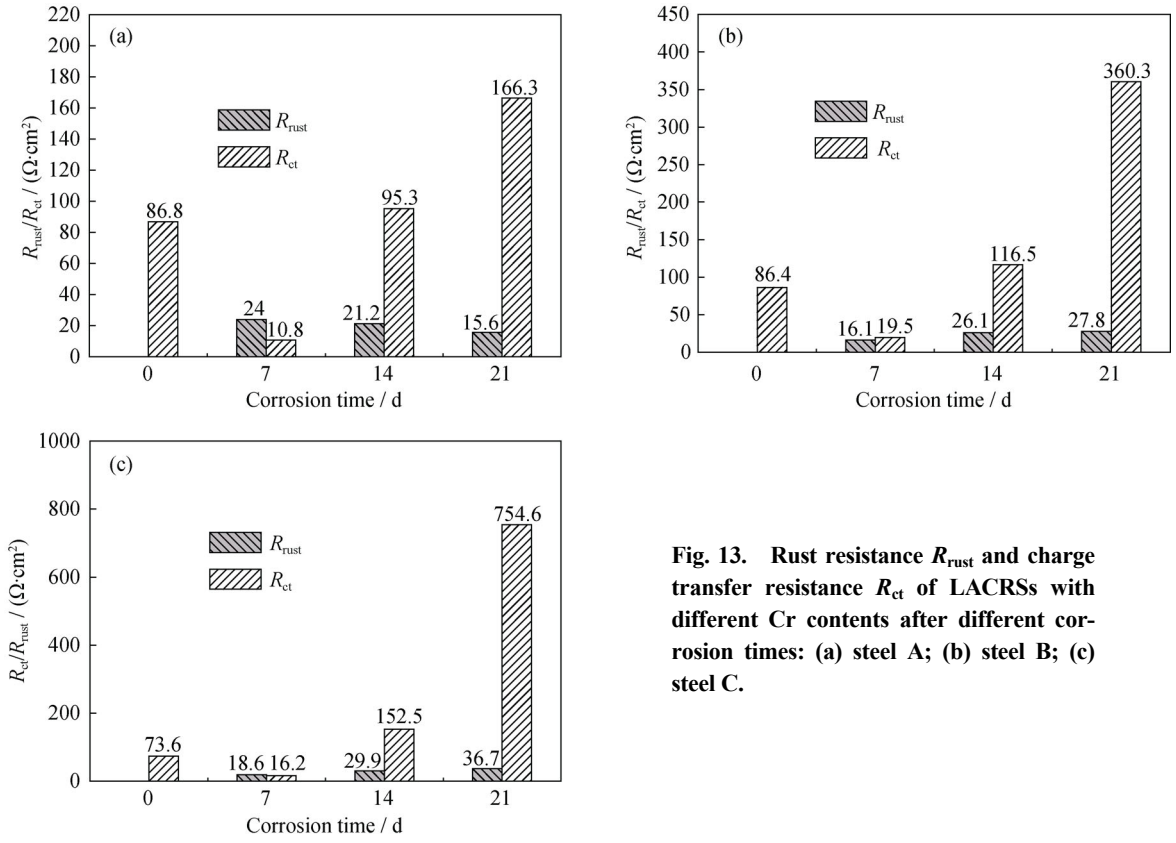

Fig. 13. Rust resistance R_{rust} and charge transfer resistance R_{ct} of LACRSs with different Cr contents after different corrosion times: (a) steel A; (b) steel B; (c) steel C.

4. Conclusions

The influence of Cr on the initial corrosion stage of low-alloy steels exposed to a CO_2–O_2–H_2S–SO_2 wet–dry cyclic corrosion environment designed to simulate that of COTs was investigated. The results led to the following conclusions.

(1) The corrosion loss and corrosion rate of steels corroded for 21 d increased with increasing Cr content, which indicates that Cr can accelerate corrosion during the initial corrosion stage.

(2) In the case of steels subjected to 21 d of corrosion, the rust grain size decreased, its SSA increased, and it became more compact and denser with increasing Cr content, which indicates that a higher Cr content promotes the formation of protective and compact rust.

(3) The amounts of α-FeOOH and γ-FeOOH decreased and the amounts of Fe_3O_4 and amorphous rust increased with increasing Cr content. The decrease in the amount of γ-FeOOH contributes to the enhanced protectivity from an electrochemical viewpoint.

(4) The EIS results indicated that R_{ct} is more reliable than R_{rust} for evaluating the protective ability of rust.

(5) Increasing Cr content accelerated the corrosion rate and promoted the formation of a protective inner rust layer during the initial corrosion stage; this protective inner rust is beneficial to lowering the long-term corrosion losses of low-alloy steels.

References

[1] H. Shiomi, M. Kaneko, K. Kashima, H. Imamura, and T. Komori, Development of anti-corrosion steel for cargo oil tanks, [in] *Proceeding of TSCF* 2007 *Shipbuilders Meeting*,

Busan, 2007, p. 1.

[2] K. Kashima, Y. Tanino, S. Kubo, A. Inami, and H. Miyuki, Development of corrosion resistant steel for cargo oil tanks, [in] *Proceeding of International Symposium on Shipbuilding Technology-Fabrication and Coatings*, Osaka, 2007, p. 5.

[3] C.G. Soares, Y. Garbatov, A. Zayed, and G. Wang, Corrosion wastage model for ship crude oil tanks, *Corros. Sci.*, 50(2008), No. 11, p. 3095.

[4] J.M. Liang, D. Tang, P.C. Zhang, H.B. Wu, H.Y. Mao, and X.T. Liu, Corrosion behavior of low-alloy steel in COT upper deck O_2–CO_2–SO_2–H_2S moisture environment, *Adv. Mater. Res.*, 652-654(2013), p. 916.

[5] Y. Yamaguchi and S. Terashima, Development of guidelines on corrosion resistant steels for cargo oil tanks, [in] *Proceeding of ASME* 2011 30*th International Conference on Ocean, Offshore and Arctic Engineering*, American Society of Mechanical Engineers, Rotterdam, 2011, p. 333.

[6] Z.F. Wang, J.R. Liu, L.X. Wu, R.D. Han, and Y.Q. Sun, Study of the corrosion behavior of weathering steels in atmospheric environments, *Corros. Sci.*, 67(2013), p. 1.

[7] H. Tamura, The role of rusts in corrosion and corrosion protection of iron and steel, *Corros. Sci.*, 50(2008), No. 7, p. 1872.

[8] D.D.N. Singh, S. Yadav, and J.K. Saha, Role of climatic conditions on corrosion characteristics of structural steels, *Corros. Sci.*, 50(2008), No. 1, p. 93.

[9] M. Kimura, T. Suzuki, G. Shigesato, H. Kihira, and K. Tanabe, $Fe(O,OH)_6$ network structure of rust formed on weathering steel surfaces and its relationship with corrosion resistance, *Nippon Steel Tech. Rep.*, 87(2003), p. 17.

[10] H.E. Townsend, Effects of alloying elements on the corrosion of steel in industrial atmospheres, *Corrosion*, 57(2001), No. 6, p. 497.

[11] W. Liu, X.H. Fan, S.F. Li, C.J. Shang, X.M. Wang, and M.X. Lu, Corrosion behavior of low alloy steels in a CO_2–O_2–H_2S–SO_2 wet gas environment of crude oil tanks, *J. Univ. Sci. Technol. Beijing*, 33(2011), No. 1, p. 33.

[12] M. Yamashita, H. Miyuki, Y. Matsuda, H. Nagano, and T. Misawa, The long term growth of the protective rust layer formed on weathering steel by atmospheric corrosion during a quarter of a century, *Corros. Sci.*, 36(1994), No. 2, p. 283.

[13] M. Yamashita, T. Shimizu, H. Konishi, J. Mizuki, and H. Uchida, Structure and protective performance of atmospheric corrosion product of Fe–Cr alloy film analyzed by Mössbauer spectroscopy and with synchrotron radiation X-rays, *Corros. Sci.*, 45(2003), No. 2, p. 381.

[14] K. Asami and M. Kikuchi, Characterization of rust layers on weathering steels air-exposed for a long period, *Mater. Trans.*, 43(2002), No. 11, p. 2818.

[15] T. Kamimura and M. Stratmann, The influence of chromium on the atmospheric corrosion of steel, *Corros. Sci.*, 43(2001), No. 3, p. 429.

[16] J.B. Sun, W. Liu, W. Chang, Z.H. Zhang, Z.T. Li, T. Yu, and M.X. Lu, Characteristics and formation mechanism of corrosion scales on low-chromium X65 steels in CO_2 environment, *Acta Metall. Sin.*, 45(2009), No. 1, p. 84.

[17] D.P. Li, L. Zhang, J.W. Yang, M.X. Lu, J.H. Ding, and M.L. Liu, Effect of H_2S concentration on the corrosion behavior of pipeline steel under the coexistence of H_2S and CO_2, *Int. J. Miner. Metall. Mater.*, 21(2014), No. 4, p. 388.

[18] J.Y. Zhong, M. Sun, D.B. Liu, X.G. Li, and T.Q. Liu, Effects of chromium on the corrosion and electrochemical behaviors of ultra high strength steels, *Int. J. Miner. Metall. Mater.*, 17(2010), No. 3, p. 282.

[19] V.G. Efremenko, K. Shimizu, A.P. Cheiliakh, T.V. Kozarevskaya, K. Kusumoto, and K. Yamamoto, Effect of vanadium and chromium on the microstructural features of V–Cr–Mn–Ni sopheroidal carbide cast irons, *Int. J. Miner. Metall. Mater.*, 21(2014), No. 11, p. 1096.

[20] X.D. Huo, Y.Q. Li, Y.T. Zhao, H.W. Zhang, and Z.H. Li, Effect of cooling parameters on the microstructure and properties of Mo-bearing and Cr-bearing steels, *Int. J. Miner. Metall. Mater.*, 18(2011), No. 5, p. 551.

[21] J. Guo, S.W. Yang, C.J. Shang, Y. Wang, and X.L. He, Influence of carbon content and microstructure on corrosion behaviour of low alloy steels in a Cl^- containing environment, *Corros. Sci.*, 51(2008), No. 2, p. 242.

[22] T. Kamimura, S. Hara, H. Miyuki, M. Yamashita, and H. Uchida, Composition, protective ability of rust layer formed on weathering steel exposed to various environments, *Corros. Sci.*, 48(2006), No. 9, p. 2799.

[23] F.R. Pérez, C.A. Barrero, O. Arnache, L.C. Sánchez, K.E. García, and A.R.H. Walker, Structural properties of iron phases formed on low alloy steels immersed in sodium chloride-rich solutions, *Phys. B*, 404(2009), No. 8-11, p. 1347.

[24] F.R. Pérez, C.A. Barrero, A.R. Hight Walker, K.E. García, and K. Nomura, Effects of chloride concentration, immersion time and steel composition on the spinel phase formation, *Mater. Chem. Phys.*, 117(2009), No. 1, p. 214.

[25] W. Ke and J.H. Dong, Study on the rusting evolution and the performance of resisting to atmospheric corrosion for Mn–Cu steel, *Acta Metall. Sin.*, 46(2010), No. 11, p. 1365.

[26] L. Hao, S.X. Zhang, J.H. Dong, and W. Ke, A study of the evolution of rust on Mo–Cu-bearing fire-resistant steel submitted to simulated atmospheric corrosion, *Corros. Sci.*, 54(2012), p. 244.

[27] K. Aasmi and M. Kikuchi, In-depth distribution of rusts on a plain carbon steel and weathering steels exposed to coastal-indutrial atmosphere for 17 years, *Corros. Sci.*, 45(2003), No. 11, p. 2671.

[28] T. Ishikawa, T. Yoshida, K. Kandori, T. Nakayama, and S. Hara, Assessment of protective function of steel rust layers by N_2 adsorption, *Corros. Sci.*, 49(2007), No. 3, p. 1468.

[29] L. Hao, S.X. Zhang, J.H. Dong, and W. Ke, Evolution of atmospheric corrosion of MnCuP weathering steel in a simulated coastal-industrial atmosphere, *Corros. Sci.*, 59(2012), p. 270.

[30] S. Hœrlé, F. Mazaudier, P. Dillmann, and G. Santarini, Advances in understanding atmospheric corrosion of iron. Ⅱ. Mechanistic modelling of wet–dry cycles, *Corros. Sci.*,

46(2004), No. 6, p. 1431.

[31] Y.H. Qian, D. Niu, J.J. Xu, and M.S. Li, The influence of chromium content on the electrochemical behavior of weathering steels, *Corros. Sci.*, 71(2013), p. 72.

[32] T. Kamimura, S. Nasu, T. Segi, T. Tazaki, S. Morimoto, and H. Miyuki, Corrosion behavior of steel under wet and dry cycles containing Cr^{3+} ion, *Corros. Sci.*, 45(2003), No. 8, p. 1863.

[33] M. Yamashita, H. Konishi, J. Mizuki, and H. Uchida, Nanostructure of protective rust layer on weathering steel examined using synchrotron radiation X-rays, *Mater. Trans.*, 45(2004), No. 6, p. 1920.

[34] M. Yamashita, H. Konishi, T. Kozakura, J. Mizuki, and H. Uchida, *In-situ* observation of initial rust formation process on carbon steel under $NaSO_4$ and NaCl solution films with wet/dry cycles using synchrotron radiation X-rays, *Corros. Sci.*, 47(2005), No. 10, p. 2492.

[35] T. Ishikawa, K. Takeuchi, K. Kandori, and T. Nakayama, Transformation of γ-FeOOH to α-FeOOH in acidic solutions containing metal ions, *Colloids Surf. A*, 266(2005), No. 1-3, p. 155.

[36] J. Majzlan, K. Grevel, and A. Navrotsky, Thermodynamics of Fe oxides: Part II. Enthalpies of formation and relative stability of goethite (α-FeOOH), lepidocrocite (γ-FeOOH), and maghemite (γ-Fe_2O_3), *Am. Mineral.*, 88(2003), No. 5-6, p. 855.

[37] H. Antony, L. Legrand, L. Maréchal, S. Perrin, Ph. Dillmann, and A. Chaussé, Study of lepidocrocite γ-FeOOH electrochemical reduction in neutral and slightly alkaline solutions at 25°C, *Electrochim. Acta*, 51(2005), No. 4, p. 745.

[38] Ph. Dillmann, F. Mazaudier, and S. Hœrlé, Advances in understanding atmospheric corrosion of iron: I. Rust characterisation of ancient ferrous artefacts exposed to indoor atmospheric corrosion, *Corros. Sci.*, 46(2004), No. 6, p. 1401.